Structure-guided mutagenesis of OSCAs reveals differential activation to mechanical stimuli

Sebastian Jojoa-Cruz[1], Adrienne E. Dubin[2], Wen-Hsin Lee[1], Andrew Ward[1]†

Affiliations

[1] Department of Integrative Structural and Computational Biology, Scripps Research, La Jolla, California 92037, USA.

[2] Department of Neuroscience, Scripps Research, La Jolla, California 92037, USA.

†Corresponding author

Correspondence to: A.B.W.: andrew@scripps.edu

Abstract (150-200 words)

The dimeric two-pore OSCA/TMEM63 family has recently been identified as mechanically activated ion channels. Previously, based on the unique features of the structure of OSCA1.2, we postulated the potential involvement of several structural elements in sensing membrane tension[1]. Interestingly, while OSCA1, 2, and 3 clades are activated by membrane stretch in cell-attached patches (i.e., they are stretch-activated channels), they differ in their ability to transduce membrane deformation induced by a blunt probe (poking). In an effort to understand the domains contributing to mechanical signal transduction, we used cryo-electron microscopy to solve the structure of *Arabidopsis thaliana* (At) OSCA3.1, which, unlike AtOSCA1.2, only produced stretch- but not poke-activated currents in our initial characterization[2]. Mutagenesis and electrophysiological assessment of conserved and divergent putative mechanosensitive features of OSCA1.2 reveal a selective disruption of the macroscopic currents elicited by poking without considerable effects on stretch-activated currents (SAC). Our results support the involvement of the amphipathic helix and lipid-interacting residues in the membrane fenestration in the response to poking. Our findings position these two structural elements as potential sources of functional diversity within the family.

30 **Introduction**

31 Mechanotransduction allows organisms to gather information about their external surroundings
32 as well as internal processes. Mechanically-activated (MA) ion channels are capable of sensing
33 mechanical stimuli and transducing this information to the cell as electrochemical signals[3]. MA
34 ion channels are diverse and capable of responding to different stimuli such as osmotic stress,
35 membrane deformation, touch, and hearing[3,4].

36

37 In our previous work, we identified OSCA/TMEM63 as a conserved family of MA ion channels
38 spanning several eukaryotic clades and having considerable diversity in the plant kingdom, where
39 species commonly have more than one paralog. For example, *Arabidopsis thaliana* has 15
40 members[2] and *Oryza sativa* L. *japonica* (rice), 11[5]. We demonstrated these channels can respond
41 to membrane stretch even more robustly than hypertonicity, originally thought to be the relevant
42 stimulus, with some members (OSCA1.1 and OSCA1.2) also able to respond to poke[2]. We used
43 cryo-electron microscopy (cryo-EM) to solve the structure of OSCA1.2 in a closed state in both
44 detergent (LMNG) and nanodiscs at high-resolution, identifying a new architecture for MA ion
45 channels that is structurally homologous to TMEM16 proteins[1]. Results from other groups are
46 consistent with ours[6-8]. Similar to the TMEM16 family, OSCAs are dimeric and each subunit has a
47 pore lined by transmembrane helices (TMs) 3 to 7, instead of a single pore along the symmetry
48 axes[1,6-8]. A hydrophobic gate on the extracellular half of the pore blocks ion flow. Additionally,
49 molecular dynamics (MD) simulations support our placement of the pore and position lipids along
50 an opening of the pore pathway in the transmembrane domain (TMD)[1].

51

52 Based on the unique structural characteristics of OSCA1.2, we proposed that two features might
53 be involved in sensing membrane deformation: the amphipathic helix (AH) located in the first
54 intracellular loop, and the Beam-Like Domain (BLD), composed of the two cytoplasmic
55 membrane-parallel helices and a hydrophobic hook that connects them and re-inserts itself into
56 the membrane[1]. Due to the close association of these two elements to the membrane, we
57 reasoned that they could serve as sensors of mechanical stimuli and transmit the signal to the
58 pore through interactions with the TMD. Additionally, a fenestration allows the membrane

access to the pore, and MD simulations placed lipids in close association with four positively charged residues in this area suggesting a potential role in gating[1]. We sought to determine whether these regions contributed to mechanotransduction.

Here, we used cryo-EM to determine a high-resolution structure of AtOSCA3.1, the first reported OSCA gene[9], in nanodiscs. In our initial characterization, OSCA3.1 responded to stretch but not poke[2]. Comparison of the OSCA3.1 structure reported here to previous structures of OSCA1.1[6] and OSCA1.2[1] revealed subtle differences. Structure-function analyses revealed the involvement of the AH and the lipid-interacting residues in the pore pathway of OSCA1.2 in the ability of the channel to respond to membrane deformation by poking. Our results suggests that these features are not only important for mechanosensation in OSCAs but may serve to tune the response of OSCA/TMEM63 members to diverse stimuli.

Results

Overall architecture of OSCA3.1 is similar to OSCA1.1 and OSCA1.2

We recombinantly tagged OSCA3.1 with EGFP at its C-terminus, expressed the construct in HEK293F cells, and purified it using Lauryl Maltose Neopentyl Glycol (LMNG) supplemented with cholesteryl hemisuccinate (CHS). The EGFP was removed by PreScission Protease cleavage, leaving a stretch of ten residues on the C-terminus. Purified protein was then reconstituted into nanodiscs and subjected to cryo-EM analysis, resulting in a 2.6 Å resolution symmetric reconstruction (Fig. 1a, Supplementary Fig. 1) sufficient to build a model of the majority of the protein (537 out of 724 residues) (Fig. 1b-c, Supplementary Fig. 2, Supplementary Table 1). Due to increased flexibility of the BLD relative to previous OSCA structures, we were unable to assign residue identity, and instead modeled it as two poly-Ala helices.

Overall, there is good agreement between OSCA3.1, OSCA1.1 and OSCA1.2 protomers[1,6] (Fig. 1c). The pore profile of these OSCAs is maintained and the small radii towards the extracellular side suggests these channels are in a closed/non-conductive state, as suggested by previous MD

88 simulations[1,6] (Fig. 1d). Likewise, the two π-helical turns in TM5 and TM6a seen in previous
89 structures near the neck of the pore are present at similar positions in OSCA3.1[1,8]. We identified
90 multiple lipid-like densities in one of our postprocessed maps (Fig. 1d, Supplementary Fig. 3).
91 Notably, one of these densities is located at the pore fenestration, at a position similar to that
92 observed in previous MD simulations of OSCA1.2[1], supporting the proposed occupation of the
93 pore pathway by lipids. Recent cryo-EM structures of AtOSCA1.2[10], and AtOSCA1.1 and human
94 TMEM63A[11] also place a lipid at a similar position.
95
96 Previously, the structure of OSCA3.1 was solved in a digitonin micelle[6], and more recently, in
97 LMNG[11]. The similarity of our nanodisc sample to these detergent structures suggests that the
98 use of detergent did not affect the conformation or oligomerization of OSCA3.1, similar to
99 previous results with OSCA1.2[1,7] (Supplementary Fig. 4a-b). However, the inter-subunit cleft in
100 the nanodisc structure is wider due to outward movements of innermost TMs ranging from ~4-
101 8Å (Supplementary Fig. 4c) relative to the digitonin sample, which was recently denoted as an
102 "extended" state[11]. Thus, our nanodisc structure represents a further "extended" state than the
103 one found both in digitonin and LMNG micelles[11] (Supplementary Fig. 4d). Whether these
104 differences represent biologically meaningful states, an effect of the lipid environment
105 (detergent vs lipids), or inherent flexibility of the channel remains to be determined. Additionally,
106 our structure enabled a higher degree of certainty in the residue assignment relative to the initial
107 digitonin structure, particularly for TM0 where sidechains were not previously modelled[6].
108 Consequently, we have shifted the registry of TM0 by two residues relative to the detergent
109 structure, in agreement with the LMNG structures[11].
110
111 **Mutation of key residues in the amphipathic helix abrogates poke but not stretch responses in**
112 **OSCA1.2**
113 Structures of AtOSCA1.1, rice and At OSCA1.2, and OSCA3.1 (Fig. 2a, Supplementary Fig. 5), as
114 well as sequence alignment, suggest that the AH between TM0 and TM1 of OSCAs is a conserved
115 feature of these channels. AHs can serve as both membrane anchors and sensors of membrane
116 deformation[12], and they are present in many MA ion channels[1,13-15]. There is evidence for their

117 involvement in mechanical force transduction; for example, in MscL, an AH in the cytoplasmic
118 side of the bilayer links membrane tension to protein conformation[14]. Interestingly, structures of
119 members of the TMEM16 family, structural homologs of OSCAs, have a similarly placed helix in
120 this region; however, it is located in the cytosol and does not present amphipathic properties
121 (Supplementary Fig. 6)[16-18]. Involvement of TMEM16A in the detection of mechanical forces in
122 myocytes and bile ducts was dependent on calcium influx (potentially caused by an upstream MA
123 cation channel) and not a direct response to the mechanical stimulus[19,20]. To our knowledge,
124 characterization of TMEM16 proteins as MA ion channels has not been reported. Based on these
125 observations, we mutated the membrane-facing residues at each end of the AH of OSCA1.2 in an
126 effort to decrease its propensity to interact with the membrane. Single (W75K or L80E) and
127 double (W75K/L80E) mutants in OSCA1.2 strongly abrogated the response to indentation of the
128 membrane with a blunt glass probe (poke) (WT: 47 of 51 cells produced MA currents; W75K: 3 of
129 24; L80E: 2 of 16; W75K/L80E: 2 of 24; Fig. 2b, top panel). Moreover, in OSCA1.2$_{W75K/L80E}$, a larger
130 displacement of the membrane by the probe relative to the WT appeared to be needed to
131 observe currents ("apparent threshold"; WT: 5.3 ± 0.5 µm (N = 46; mean ± S.E.M.), W75K/L80E:
132 15.3 ± 2.3 µm (N = 2); Fig. 2b, bottom panel). The insensitivity to the poking stimulus was not due
133 to poor membrane trafficking of these constructs (see below). The loss of sensitivity of cells
134 expressing these mutant constructs to poking suggests that the AH of OSCA1.2 plays an important
135 role in this mechanically-activated response.
136
137 We then tested whether these mutations in the AH affected the response of OSCA1.2 to stretch.
138 Contrary to what was observed during poking, all cell-attached patches revealed stretch-
139 activated currents (WT: 25 of 26 cells; W75K: 3 of 3; L80E: 5 of 5; W75K/L80E: 11 of 11; Fig. 2c,
140 top panel; electrode resistances were similar in all cases (see Figure legend)). Despite differences
141 in the amplitude of macroscopic currents, which could be explained by variation in expression
142 levels, all mutant channels were activated at similar thresholds (WT: -48 ± 5 mmHg (N = 25);
143 W75K: -56 ± 11 mmHg (N = 3), L80E: -41 ± 6 mmHg (N = 5), W75K/L80E: -53 ± 8 mmHg (N = 11))
144 (Fig. 2c, bottom panel). In all cases, there was variability in the rate of inactivation from

145 moderately fast to extremely slow (data not shown). Overall, the observed stretch response of
146 OSCA1.2 was apparently not affected by the mutations we introduced.
147
148 Subsequently, we mutated the proline in the OSCA1.2 AH to the corresponding arginine in
149 OSCA3.1 to determine whether this difference impacts the ability of OSCA3.1 to robustly
150 transduce the poke stimulus; this change (OSCA1.2$_{P77R}$) had no effect on the poke response
151 (Supplementary Fig. 7).
152
153 It is worth noting that in our initial characterization, OSCA3.1-expressing cells produced SAC while
154 poke did not induce observable currents[2]. However, in the present experiments we were able to
155 record poke-activated currents mediated by OSCA3.1 on a few occasions (OSCA1.2$_{WT}$: 6 of 6 cells;
156 OSCA3.1$_{WT}$: 3 of 10) (Supplementary Fig. 8a). The apparent threshold for OSCA3.1 activation by
157 poke-induced membrane displacement tended to be higher than for OSCA1.2 but the difference
158 was not statistically significant (OSCA1.2$_{WT}$: 10.4 ± 1.2 µm (N = 6; mean ± S.E.M.); OSCA3.1$_{WT}$:
159 13.8 ± 0.9 µm (N = 3)) (Supplementary Fig. 8b), perhaps due to the low numbers of responsive
160 cells analyzed. These data suggest that the poking stimulus is capable of activating OSCA3.1 but
161 the stimulus intensity required is close to the rupture point of the HEK293T-Piezo1-knockout
162 (HEK-P1KO) cells used in our assay.
163
164 **Replacing the OSCA3.1 Beam-Like Domain (BLD) in OSCA1.2 had no effect on stretch-induced**
165 **currents but decreased the apparent sensitivity of the cells to poke**
166 One of the unique features of OSCAs is the presence of the BLD, a hydrophobic hook that, by
167 inserting itself into the membrane, may serve as an anchor that could potentially be displaced
168 under tension[1,7,8]. Hydrogen/deuterium exchange mass spectrometry (HDXMS) of rice OSCA1.2
169 indicated that the helix of the BLD closest to the membrane undergoes less deuterium exchange
170 and potentially remains associated to a neighboring surface[8], hinting at an important interaction
171 with TM6b. In OSCA3.1, the BLD is poorly resolved, likely due to flexibility (Fig. 1c). To test
172 whether the increased flexibility in this region affects MA responses, we replaced the BLD of
173 OSCA1.2 with the BLD of OSCA3.1 (Fig. 3a). HEK-P1KO cells expressing the chimera OSCA1.2$_{OSCA3.1-}$

174 $_{BLD}$ produced similar MA currents in both poke and stretch assays (Fig. 3b,c) with the exception
175 that a slightly stronger displacement stimulus was required to activate the mutant channels (Fig.
176 3b, bottom panel). These data suggest that the BLD is not responsible on its own for the ability
177 of the channels to be activated by poking, however, it appears to play a role. As expected for
178 similar SAC from cells expressing OSCA1.2 and OSCA3.1, there was no obvious change in SAC
179 when the OSCA1.2 BLD was replaced with the OSCA3.1 BLD. It should be noted that the BLD
180 tolerates a certain degree of mutation as sequence alignment in this region shows higher
181 variability than other secondary structures of OSCAs (Supplementary Fig. 5). Thus, we cannot rule
182 out that in the OSCA1.2 background, the BLD of either channel is capable of performing a similar
183 role.
184
185 **Substitution of potential lipid-interacting lysine residues for isoleucine abrogates the poke**
186 **response in OSCA1.2**
187 Lipids play an important role in the stability and function of ion channels[21]. In TRAAK, a eukaryotic
188 mechanosensitive channel, occlusion of the pore by a lipid acyl chain has been proposed as a
189 gating mechanism[13,22]. In the volume-regulated channel SWELL1 lipids block the pore in the
190 closed state[23]. In the bacterial mechanosensitive channel MscS, the occupation of lipid pockets
191 may determine channel conformation[24,25], and in FLYC1, a Venus flytrap homolog of MscS,
192 conformational changes may allow lipids to access the pore and occlude ion conduction[26].
193 Moreover, exposure of inside-out patches from OSCA1.1-expressing HEK cells to lyso-
194 phosphatyidylcholine (LPC) enhanced channel response to stretch[6].
195
196 Previously, we identified four lysine residues in OSCA1.2 located in TM4 and TM6b at the pore
197 fenestration. These residues interacted with lipid phosphate head groups throughout the
198 duration of our MD simulations[1]. The OSCA3.1 structure revealed that two of these lysine
199 residues (K435 and K536 of OSCA1.2) have been replaced by isoleucine (I423 and I525,
200 respectively), which are expected to reduce the interaction with lipid phosphate head groups
201 (Fig. 4a). To test for the contribution of these lipid-interacting residues to channel
202 mechanosensitivity, we measured poke- and stretch-induced currents in the double mutant

203 OSCA1.2$_{K435I/K536I}$ (Fig. 4b,c). The double mutant responded poorly to poking, with only 1 out of
204 20 cells producing currents upon mechanical stimulation (K435I/K536I: -365 pA (N = 1)) (Fig. 4b,
205 comparison made to WT data acquired on the same days). This finding was not due to poor
206 expression of the double mutant in HEK-P1KO cells; the SAC I_{max} observed in cell-attached patches
207 was similar to WT (Fig. 4c, top panel). Furthermore, the mutant could be activated by stretch at
208 similar thresholds to WT (WT: -43 ± 10 mmHg (N = 6); K435I/K536I: -60 ± 10 mmHg (N = 7)) (Fig.
209 4c, bottom panel), and similar stretch-response dependence (i.e., similar pressures required to
210 elicit half-maximal currents (P_{50}) and slope) (Fig. 4d). Although macrocurrent amplitudes in SAC
211 recordings tended to be lower than WT tested on the same day, the ~2-fold difference unlikely
212 accounts for the ~20-fold fewer responsive cells (Fig. 4b,c). Taken together, these results suggest
213 that loss of positively charged sidechains in the fenestration selectively impairs poke-induced
214 responses of OSCA1.2 under physiological conditions, but not its responsiveness to the stretch
215 stimulus.
216
217 **Discussion**
218 Here we performed structure-function studies to determine the molecular underpinnings of
219 mechanical activation of OSCA ion channels. We solved the structure of OSCA3.1 at a resolution
220 of 2.6 Å in a non-conductive state and revealed a marked structural conservation to previous
221 OSCA orthologs. The final map presented several lipid-like densities surrounding the channel,
222 including one density close to the pore and several densities populating the inter-subunit cleft.
223 This ion channel was reported to be activated by stretch in cell-attached patches but insensitive
224 to a poke stimulus using a blunt glass probe[2]. Comparisons between the structures of OSCA1.2,
225 which is robustly activated by both poke and stretch, to OSCA3.1, which is only robustly
226 activated by stretch, suggested 3 domains that might contribute to gating during a poke
227 stimulus. First, a conserved short amphipathic helix (AH) which sits at the membrane interface
228 reminiscent of a similar feature in other MA ion channels like MscL[14], Piezo1[15], MscS[27], and
229 TRAAK[28]. Second, side chains in TM4 and TM6b in the vicinity of the membrane fenestration
230 may have differential interactions with lipids as indicated by MD simulations of OSCA1.2. Third,
231 the beam-like domain (BLD) that contains 2 helices and linker that hooks around the

232 cytoplasmic surface into the membrane in OSCA1.2 but is less well-resolved in the OSCA3.1
233 map presumably because it is not intimately associated with the channel/membrane.
234 Mutagenesis of the AH and residues at the fenestration in OSCA1.2 largely abrogated its
235 response to poking without affecting its activation by stretch; replacing the BLD with that from
236 OSCA3.1 only slightly impaired the response to poking, having no effect on stretch-induced
237 activation.
238
239 Residues in the AH were mutated to either confer more of an OSCA3.1 character or tend to
240 make the domain less likely to interact with the membrane, similar to the TMEM16 family that
241 are not thought to be directly activated by mechanical stimuli. Swapping the divergent residue
242 in the AH of OSCA1.2 with its equivalent in OSCA3.1 (OSCA1.2$_{P77R}$), had no negative impact on
243 the sensitivity to poking. However, when mutations were incorporated to presumably
244 destabilize the interaction of the AH domain with the membrane (OSCA1.2$_{W75K/L80E}$), fewer cells
245 could be activated by poking to similar stimulus strengths while stretch-activation of channels
246 was not impaired. Although a WT AH is critical for normal poke-induced channel opening, these
247 mutations do not hinder gating by membrane stretch.
248
249 Substituting the BLD of OSCA1.2 for that of OSCA3.1 had little effect on poke- or stretch-
250 activated responses. Although these results suggest that the BLD may not be involved in
251 modulating the MA response of OSCA1.2, a recent report suggested evolutionary coupling of 3
252 sets of residues in the BLD and TM6b that may form electrostatic interactions between these
253 domains[10]. The evolutionarily favored residue identities at these sites constitute three potential
254 salt bridges: **R/K**257-**E**557, **E**260-**R**553, and **R/K**261-**E/D**554 (based on OSCA1.2 numbering).
255 These sites in OSCA1.2$_{OSCA3.1\text{-}BLD}$ chimera correspond to N257**K**-**E**557, D260**A**-**K**553, and Y261**R**-
256 **D**554 (mutation-interacting residue), perhaps leaving intact 2 out of 3 potential salt bridges and
257 maintaining its influence (Supplementary Fig. 5). It is worth noting that a similar chimera of
258 AtOSCA1.2 with the IL2 domain of the human ortholog TMEM63A (OSCA1.2$_{63A\ IL2}$), containing
259 most of the intracellular domain which includes the BLD as well as the dimerization domain,
260 presented little inactivation of SAC akin to monomeric TMEM63A$_{WT}$[29]. This behavior was not

261 due to an inability of OSCA1.2$_{63A\ IL2}$ to dimerize, as the monomeric OSCA1.2$_{5Mu}$, obtained by
262 disrupting the dimer interface with 5 mutations while maintaining OSCA1.2$_{WT}$ BLD, exhibited
263 pressure-induced SAC gating similar to OSCA1.2$_{WT}$[29]. This new evidence, taken together with
264 the decrease in the apparent poking sensitivity of the OSCA1.2$_{OSCA3.1\text{-}BLD}$ chimera in this study,
265 suggests that the BLD plays a role in the force-induced gating of the OSCA family.
266
267 The structure of OSCA3.1 exhibits an open fenestration similar to OSCA1.2 and lipids are expected
268 to populate this area[1], similar to lipid occlusion of the pore in other MA ion channels such as
269 TRAAK[13] and MscS[24,25]. Our results suggest that TM4 and TM6b interactions with lipids may
270 contribute to activation during poking. Modification of OSCA1.2 residues to match those of
271 OSCA3.1 (OSCA1.2$_{K435I/K536I}$) produced an OSCA3.1-like phenotype (MA currents are observed in
272 response to stretch but rarely to poke). These mutant channels are not completely insensitive to
273 poking but appear to have a very high threshold to activate, one that is often beyond the point
274 of cell rupture by the stimulus (similar to that seen with OSCA1.2$_{W75K/L80E}$). Notably, TM4 in
275 TMEM16 lipid scramblases and TM6 in both TMEM16 scramblases and channels undergo
276 conformational changes during activation[16,17,30]. The loss of positive charges in OSCA3.1 may
277 weaken the interactions between residues and lipids, similar to MscS where charge
278 neutralization of the lipid facing residue R59 by introduction of a leucine strongly altered gating,
279 potentially by disturbing a salt bridge with a lipid phosphate[31,32]. A weaker interaction could
280 decrease the tension generated by the lipids upon mechanical stimulus, hence increasing the
281 force needed to open the channel, as seen in our poke experiments. A similar argument could be
282 made for the AH of OSCAs: by disturbing its coupling with the lipid bilayer, a greater stimulus
283 might be needed to activate the channel.
284
285 The phenotypes of OSCA1.2$_{W75K/L80E}$ and OSCA1.2$_{K435I/K536I}$ suggest a mechanism recruited by
286 poking is no longer able to adequately activate OSCA1.2$_{W75K/L80E}$ and OSCA1.2$_{K435I/K536I}$ channels.
287 Since the factors contributing to channel activation in the poking assay are not understood, we
288 can only speculate as to mechanisms underlying the loss of sensitivity to poking in these mutants.
289 Our results suggest that these stimuli are sensed by different features of OSCA channels, akin to

290 the well-studied ThermoTRP channels[33-35]. Polymodal activation mechanisms have been recently
291 reported for the MA channel PIEZO2 where a mutagenesis approach revealed differential effects
292 on the ability to respond to poking and stretch[36]. Nonetheless, the discrepancy could be due to
293 inherent methodological differences between these two assays, as whole-cell recordings during
294 poking involve channels in inaccessible membranes (at the cell-substrate interface) and channel
295 interactions with extracellular and intracellular components[37], while the stretch assay is limited
296 to recording channels inside the patch.
297
298 Overall, the analysis of these mutants demonstrates the involvement of the AH and residues at
299 the membrane fenestration in the MA response of OSCAs, as we initially proposed[1]. The
300 participation of residues from TM4 and TM6 hint at further similarities with TMEM16 family, but
301 to what extent is unknown. Perhaps the most surprising result is the selective disruption of poke-
302 activated currents of OSCA1.2 without affecting its response to membrane stretch, which
303 suggests that changes in these features could serve to fine-tune the response to certain
304 mechanical stimuli and may be a source of functional diversity within this large family. The
305 structures and characterizations presented here and in our previous work[1,2] will prove
306 fundamental in assessing the physiological consequences of these differences and further
307 understanding the role of the OSCA/TMEM63 family.
308
309
310
311 **Materials and methods:**
312 Expression constructs
313 For structural studies, human codon-optimized OSCA3.1 (UniProt ID: Q9C8G5) was cloned into
314 the pcDNA3.1 vector used in our previous report[1]. In this plasmid, the C terminus of the protein
315 sequence is followed by a PreScission Protease cleavage site, EGFP and a FLAG tag.
316
317
318 Protein expression and purification

319 Samples of OSCA3.1 in nanodisc were obtained following the same method reported previously
320 for OSCA1.2 in nanodiscs[1], with the exception of the detergent used. Instead of beta-D-
321 maltopyranoside (DDM), we used Lauryl Maltose Neopentyl Glycol (LMNG) due to increased
322 yields. Thus, the detergent composition of the solubilization and wash buffers was 1%/0.1% and
323 0.01%/0.001% LMNG/cholesteryl hemisuccinate (CHS), respectively. Fractions from Size
324 Exclusion Chromatography (SEC) corresponding to the OSCA3.1 in nanodiscs peak were
325 concentrated to 3.2mg/mL (corrected using the extinction coefficient of OSCA3.1).
326
327
328 Cryo-EM sample preparation and data collection
329 3.5 µL of OSCA3.1 at 3.2mg/mL were frozen using the same conditions as OSCA1.2 samples[1].
330 Grids were imaged on a Titan Krios (ThermoFisher) operating at 300 kV with a K2 Summit direct
331 electron detector (Gatan), with pixel size of 1.03Å (nominal magnification of 29,000x). A total of
332 38 frames were collected per movie, adding to a total dose of ~50 electrons per $Å^2$. Automated
333 image collection was done through Leginon[38] using a defocus range of -0.4 to -1.5 µm. A total of
334 8,375 movies were collected.
335
336
337 Cryo-EM image processing
338 During collection, movies were aligned and dose-weighted using MotionCor2[39]. The resulting
339 micrographs were imported into cryoSPARCv2.5[40] and CTF values were estimated through Gctf[41].
340 ~300 particles were manually picked from ~10 micrographs and subjected to 2D classification to
341 obtain templates. Template picking was tested on 20 micrographs and particles used to generate
342 better 2D templates. These templates were later used to pick particles on ~1600 micrographs.
343 The resulting ~900k particles were subjected to, in order, 2D classification, *ab initio*
344 reconstruction, 2 rounds of heterogeneous refinement, homogeneous refinement and non-
345 uniform refinement to obtain an initial 3D reference, which reached high-resolution. Unless
346 otherwise specified, C2 symmetry was applied to all homogeneous, non-uniform and RELION 3D
347 refinements.

348

349 For the full dataset, 8,375 movies were imported into cryoSPARCv2 and subjected to full-frame
350 motion correction followed by Gctf estimation. Given the large size of the dataset, and the fact
351 that initial processing had returned a high-resolution structure, we decided to apply a 2.6 Å CTF
352 cutoff to reduce the number of micrographs to 3,068 and speed up processing. Templates were
353 generated based on the initial 3D reference. Template picking, followed by local motion
354 correction and 2D classification resulted in 1,913,316 selected particles for our initial stack. *Ab*
355 *initio* reconstruction produced 3 classes, and heterogeneous refinement was performed on the
356 two worst classes. The resulting best class was combined with the best class from *ab initio* and
357 used for two rounds of heterogeneous and homogeneous refinements. The heterogeneous
358 refinement of the first round was done without symmetry, from that point onwards, C2
359 symmetry was imposed unless otherwise specified. Only particles belonging to the best class
360 were selected for further processing (318,249). Non-uniform refinement, followed by 2 rounds
361 of local refinement (without imposing symmetry), were performed on these particles before
362 exporting them into RELION-3.1[42,43]. The particle stack underwent the following process in
363 RELION. 3D refinement, CTF refinement, 3D refinement with global angular searches, 3D
364 refinement using SIDESPLITTER (SS)[44], and two rounds of CTF and 3D refinements using SS. Unless
365 specified, all 3D refinements were limited to local angular searches. 3D classification without
366 alignment (no imposed symmetry) was performed on the particle stack and the best class,
367 comprising 197,944 particles, was subjected to a final 3D refinement with SS. The map was
368 sharpened separately with LocalDeblur[45] through Scipion[46-48] and DeepEMhancer using the
369 'highRes' model[49]. The FSC and local resolution of the map was calculated through RELION.

370

371

372 Model building and refinement

373 A homology model for OSCA3.1 was obtained through SWISS-MODEL[50], using as template the
374 structure of OSCA1.2 in nanodiscs (PDB: 6MGV)[1]. Iterative rounds of building in Coot[51,52] and real
375 space refinement in Phenix[53,54] and Rosetta[55] were used to generate the final model. SMILES
376 codes for the ligands were used to obtain the appropriate restrains using eLBOW[56]. Model

377 validation was carried out with MolProbity[57] and EMringer[58] to the LocalDeblur map. Phenix
378 mtriage[59] was used to calculate the map to model FSC. The final model comprises residues 2-102,
379 154-231, 307-388, 410-476, and 489-697, for a total of 537 out of 724 residues in OSCA3.1
380 sequence. A segment of the BLD was modelled as poly-A helices and registry was tentatively
381 assigned based on sequence and structure alignment to OSCA1.2[1]: residues 234-246 and 280-
382 303 assigned as IL2H2 and IL2H3, respectively. Pore profiles were predicted by CHAP[60,61].
383 Structure figures were made with PyMOL[62], UCSF Chimera[63] or UCSF ChimeraX[64]. Amino acid
384 sequence alignment was obtained from Clustal omega[65] and represented with ESPript3[66].
385 Sequences used for the alignment were the same as previous publication[1], but the display was
386 limited to the *Arabidopsis thaliana* OSCAs with solved structure.
387
388
389 Generation of mutants, cell culture and transfections
390 A vector containing OSCA1.2 pIRES2-mCherry was used for electrophysiology experiments[2]. The
391 W75K substitution was introduced using Q5 site-directed mutagenesis kit (New England Biolabs,
392 NEB). Substitutions L80E, K435I, and K536I were introduced using QuikChange multi site-directed
393 mutagenesis kit (Agilent). For the BLD chimera, OSCA1.2 pIRES2-mCherry vector and the BLD of
394 OSCA3.1 were separately amplified by PCR using Q5 High-Fidelity 2X Master Mix (NEB), followed
395 by fragment assembly using Gibson Assembly Master Mix (NEB). Kits were used according to
396 manufacturer's instructions.
397
398 Cell culture and transfection of HEK-P1KO cells for electrophysiology experiments were
399 conducted as previously reported[1].
400
401
402 Electrophysiology
403 Patch-clamp experiments in transiently transfected HEK-P1KO cells were performed in standard
404 whole-cell and cell-attached mode using a Multi-clamp700A amplifier (Axon Instruments) and
405 followed the procedures described in our previous report[2].

Data availability

Cryo-EM maps of OSCA3.1 in nanodiscs has been deposited to the Electron Microscopy Data Bank (EMDB) under accession number EMD-41911 with the LocalDeblur map as the primary map. The corresponding atomic coordinates have been deposited to the Protein Data Bank (PDB) under ID 8U53.

Author contributions:

S.J.C. and W.H.L. cloned expression constructs and mutants. S.J.C. prepared protein samples and acquired cryo-EM data. S.J.C. processed data and built and refined the atomic structures. A.E.D. carried out electrophysiology experiments and analyzed data. A.B.W. supervised the project. S.J.C. and A.E.D. drafted the manuscript, which was edited and finalized with contributions from all authors.

Acknowledgements:

We thank W. Anderson for management the electron microscopy facility at Scripps Research, J. Torres for help with data collection, and C. Bowman, L. Dong and J.C. Ducom for assistance with computation. We acknowledge members of the Ward laboratory. This work was supported by NIH grant R01 HL143297 and a Ray Thomas Edwards Foundation grant to A.B.W. A.E.D was supported by grant R35 NS105067.

Molecular graphics and analyses performed with UCSF Chimera and UCSF ChimeraX, developed by the Resource for Biocomputing, Visualization, and Informatics at the University of California, San Francisco, with support from National Institutes of Health R01-GM129325 and P41-

434 GM103311, and the Office of Cyber Infrastructure and Computational Biology, National Institute
435 of Allergy and Infectious Diseases.

436 **References**

437 1 Jojoa-Cruz, S. *et al.* Cryo-EM structure of the mechanically activated ion channel OSCA1.2.
438 *Elife* **7** (2018). https://doi.org:10.7554/eLife.41845
439 2 Murthy, S. E. *et al.* OSCA/TMEM63 are an Evolutionarily Conserved Family of Mechanically
440 Activated Ion Channels. *Elife* **7** (2018). https://doi.org:10.7554/eLife.41844
441 3 Ranade, S. S., Syeda, R. & Patapoutian, A. Mechanically Activated Ion Channels. *Neuron*
442 **87**, 1162-1179 (2015). https://doi.org:10.1016/j.neuron.2015.08.032
443 4 Haswell, E. S., Phillips, R. & Rees, D. C. Mechanosensitive Channels: What Can They Do
444 and How Do They Do It? *Structure* **19**, 1356-1369 (2011).
445 https://doi.org:10.1016/j.str.2011.09.005
446 5 Li, Y. *et al.* Genome-wide survey and expression analysis of the OSCA gene family in rice.
447 *BMC Plant Biol* **15**, 261 (2015). https://doi.org:10.1186/s12870-015-0653-8
448 6 Zhang, M. *et al.* Structure of the mechanosensitive OSCA channels. *Nat Struct Mol Biol* **25**,
449 850-858 (2018). https://doi.org:10.1038/s41594-018-0117-6
450 7 Liu, X., Wang, J. & Sun, L. Structure of the hyperosmolality-gated calcium-permeable
451 channel OSCA1.2. *Nat Commun* **9**, 5060 (2018). https://doi.org:10.1038/s41467-018-
452 07564-5
453 8 Maity, K. *et al.* Cryo-EM structure of OSCA1.2 from Oryza sativa elucidates the mechanical
454 basis of potential membrane hyperosmolality gating. *Proc Natl Acad Sci U S A* **116**, 14309-
455 14318 (2019). https://doi.org:10.1073/pnas.1900774116
456 9 Kiyosue, T., Yamaguchi-Shinozaki, K. & Shinozaki, K. Cloning of cDNAs for genes that are
457 early-responsive to dehydration stress (ERDs) in Arabidopsis thaliana L.: identification of
458 three ERDs as HSP cognate genes. *Plant Mol Biol* **25**, 791-798 (1994).
459 https://doi.org:10.1007/BF00028874
460 10 Jojoa-Cruz, S., Burendei, B., Lee, W.-H. & Ward, A. B. Structure of mechanically activated
461 ion channel OSCA2.3 reveals mobile elements in the transmembrane domain. *bioRxiv*,
462 2023.2006.2015.545135 (2023). https://doi.org:10.1101/2023.06.15.545135
463 11 Zhang, M., Shan, Y., Cox, C. D. & Pei, D. A mechanical-coupling mechanism in
464 OSCA/TMEM63 channel mechanosensitivity. *Nat Commun* **14**, 3943 (2023).
465 https://doi.org:10.1038/s41467-023-39688-8
466 12 Drin, G. & Antonny, B. Amphipathic helices and membrane curvature. *FEBS Lett* **584**,
467 1840-1847 (2010). https://doi.org:10.1016/j.febslet.2009.10.022
468 13 Brohawn, S. G., Campbell, E. B. & MacKinnon, R. Physical mechanism for gating and
469 mechanosensitivity of the human TRAAK K+ channel. *Nature* **516**, 126-130 (2014).
470 https://doi.org:10.1038/nature14013
471 14 Bavi, N. *et al.* The role of MscL amphipathic N terminus indicates a blueprint for bilayer-
472 mediated gating of mechanosensitive channels. *Nat Commun* **7**, 11984 (2016).
473 https://doi.org:10.1038/ncomms11984
474 15 Saotome, K. *et al.* Structure of the mechanically activated ion channel Piezo1. *Nature* **554**,
475 481-486 (2018). https://doi.org:10.1038/nature25453
476 16 Paulino, C., Kalienkova, V., Lam, A. K. M., Neldner, Y. & Dutzler, R. Activation mechanism
477 of the calcium-activated chloride channel TMEM16A revealed by cryo-EM. *Nature* **552**,
478 421-425 (2017). https://doi.org:10.1038/nature24652

17 Alvadia, C. *et al.* Cryo-EM structures and functional characterization of the murine lipid scramblase TMEM16F. *Elife* **8** (2019). https://doi.org:10.7554/eLife.44365

18 Bushell, S. R. *et al.* The structural basis of lipid scrambling and inactivation in the endoplasmic reticulum scramblase TMEM16K. *Nat Commun* **10**, 3956 (2019). https://doi.org:10.1038/s41467-019-11753-1

19 Bulley, S. *et al.* TMEM16A/ANO1 channels contribute to the myogenic response in cerebral arteries. *Circ Res* **111**, 1027-1036 (2012). https://doi.org:10.1161/CIRCRESAHA.112.277145

20 Dutta, A. K., Woo, K., Khimji, A. K., Kresge, C. & Feranchak, A. P. Mechanosensitive Cl-secretion in biliary epithelium mediated through TMEM16A. *Am J Physiol Gastrointest Liver Physiol* **304**, G87-98 (2013). https://doi.org:10.1152/ajpgi.00154.2012

21 Duncan, A. L., Song, W. & Sansom, M. S. P. Lipid-Dependent Regulation of Ion Channels and G Protein-Coupled Receptors: Insights from Structures and Simulations. *Annu Rev Pharmacol Toxicol* **60**, 31-50 (2020). https://doi.org:10.1146/annurev-pharmtox-010919-023411

22 Brohawn, S. G., Su, Z. & MacKinnon, R. Mechanosensitivity is mediated directly by the lipid membrane in TRAAK and TREK1 K+ channels. *Proc Natl Acad Sci U S A* **111**, 3614-3619 (2014). https://doi.org:10.1073/pnas.1320768111

23 Kern, D. M. *et al.* Structural basis for assembly and lipid-mediated gating of LRRC8A:C volume-regulated anion channels. *Nat Struct Mol Biol* **30**, 841-852 (2023). https://doi.org:10.1038/s41594-023-00944-6

24 Pliotas, C. *et al.* The role of lipids in mechanosensation. *Nat Struct Mol Biol* **22**, 991-998 (2015). https://doi.org:10.1038/nsmb.3120

25 Zhang, Y. *et al.* Visualization of the mechanosensitive ion channel MscS under membrane tension. *Nature* **590**, 509-514 (2021). https://doi.org:10.1038/s41586-021-03196-w

26 Jojoa-Cruz, S. *et al.* Structural insights into the Venus flytrap mechanosensitive ion channel Flycatcher1. *Nat Commun* **13**, 850 (2022). https://doi.org:10.1038/s41467-022-28511-5

27 Reddy, B., Bavi, N., Lu, A., Park, Y. & Perozo, E. Molecular basis of force-from-lipids gating in the mechanosensitive channel MscS. *Elife* **8** (2019). https://doi.org:10.7554/eLife.50486

28 Brohawn, S. G., del Marmol, J. & MacKinnon, R. Crystal structure of the human K2P TRAAK, a lipid- and mechano-sensitive K+ ion channel. *Science* **335**, 436-441 (2012). https://doi.org:10.1126/science.1213808

29 Zheng, W. *et al.* TMEM63 proteins function as monomeric high-threshold mechanosensitive ion channels. *Neuron* (2023). https://doi.org:10.1016/j.neuron.2023.07.006

30 Kalienkova, V. *et al.* Stepwise activation mechanism of the scramblase nhTMEM16 revealed by cryo-EM. *Elife* **8** (2019). https://doi.org:10.7554/eLife.44364

31 Flegler, V. J. *et al.* Mechanosensitive channel gating by delipidation. *Proc Natl Acad Sci U S A* **118** (2021). https://doi.org:10.1073/pnas.2107095118

32 Rasmussen, T. *et al.* Interaction of the Mechanosensitive Channel, MscS, with the Membrane Bilayer through Lipid Intercalation into Grooves and Pockets. *J Mol Biol* **431**, 3339-3352 (2019). https://doi.org:10.1016/j.jmb.2019.05.043

33 Fernandez-Ballester, G., Fernandez-Carvajal, A. & Ferrer-Montiel, A. Progress in the Structural Basis of thermoTRP Channel Polymodal Gating. *Int J Mol Sci* **24** (2023). https://doi.org:10.3390/ijms24010743

34 Jordt, S. E. & Julius, D. Molecular basis for species-specific sensitivity to "hot" chili peppers. *Cell* **108**, 421-430 (2002). https://doi.org:10.1016/s0092-8674(02)00637-2

35 Bandell, M. *et al.* High-throughput random mutagenesis screen reveals TRPM8 residues specifically required for activation by menthol. *Nat Neurosci* **9**, 493-500 (2006). https://doi.org:10.1038/nn1665

36 Verkest, C. *et al.* Intrinsically disordered intracellular domains control key features of the mechanically-gated ion channel PIEZO2. *Nat Commun* **13**, 1365 (2022). https://doi.org:10.1038/s41467-022-28974-6

37 Richardson, J., Kotevski, A. & Poole, K. From stretch to deflection: the importance of context in the activation of mammalian, mechanically activated ion channels. *FEBS J* (2021). https://doi.org:10.1111/febs.16041

38 Suloway, C. *et al.* Automated molecular microscopy: the new Leginon system. *J Struct Biol* **151**, 41-60 (2005). https://doi.org:10.1016/j.jsb.2005.03.010

39 Zheng, S. Q. *et al.* MotionCor2: anisotropic correction of beam-induced motion for improved cryo-electron microscopy. *Nat Methods* **14**, 331-332 (2017). https://doi.org:10.1038/nmeth.4193

40 Punjani, A., Rubinstein, J. L., Fleet, D. J. & Brubaker, M. A. cryoSPARC: algorithms for rapid unsupervised cryo-EM structure determination. *Nat Methods* **14**, 290-296 (2017). https://doi.org:10.1038/nmeth.4169

41 Zhang, K. Gctf: Real-time CTF determination and correction. *J Struct Biol* **193**, 1-12 (2016). https://doi.org:10.1016/j.jsb.2015.11.003

42 Scheres, S. H. RELION: implementation of a Bayesian approach to cryo-EM structure determination. *J Struct Biol* **180**, 519-530 (2012). https://doi.org:10.1016/j.jsb.2012.09.006

43 Zivanov, J., Nakane, T. & Scheres, S. H. W. Estimation of high-order aberrations and anisotropic magnification from cryo-EM data sets in RELION-3.1. *IUCrJ* **7**, 253-267 (2020). https://doi.org:10.1107/S2052252520000081

44 Ramlaul, K., Palmer, C. M., Nakane, T. & Aylett, C. H. S. Mitigating local over-fitting during single particle reconstruction with SIDESPLITTER. *J Struct Biol* **211**, 107545 (2020). https://doi.org:10.1016/j.jsb.2020.107545

45 Ramirez-Aportela, E. *et al.* Automatic local resolution-based sharpening of cryo-EM maps. *Bioinformatics* **36**, 765-772 (2020). https://doi.org:10.1093/bioinformatics/btz671

46 Vilas, J. L. *et al.* MonoRes: Automatic and Accurate Estimation of Local Resolution for Electron Microscopy Maps. *Structure* **26**, 337-344 e334 (2018). https://doi.org:10.1016/j.str.2017.12.018

47 de la Rosa-Trevin, J. M. *et al.* Xmipp 3.0: an improved software suite for image processing in electron microscopy. *J Struct Biol* **184**, 321-328 (2013). https://doi.org:10.1016/j.jsb.2013.09.015

48 de la Rosa-Trevin, J. M. *et al.* Scipion: A software framework toward integration, reproducibility and validation in 3D electron microscopy. *J Struct Biol* **195**, 93-99 (2016). https://doi.org:10.1016/j.jsb.2016.04.010

49 Sanchez-Garcia, R. *et al.* DeepEMhancer: a deep learning solution for cryo-EM volume post-processing. *Commun Biol* **4**, 874 (2021). https://doi.org:10.1038/s42003-021-02399-1

50 Waterhouse, A. *et al.* SWISS-MODEL: homology modelling of protein structures and complexes. *Nucleic Acids Res* **46**, W296-W303 (2018). https://doi.org:10.1093/nar/gky427

51 Emsley, P. & Cowtan, K. Coot: model-building tools for molecular graphics. *Acta Crystallogr D* **60**, 2126-2132 (2004). https://doi.org:10.1107/S0907444904019158

52 Casanal, A., Lohkamp, B. & Emsley, P. Current developments in Coot for macromolecular model building of Electron Cryo-microscopy and Crystallographic Data. *Protein Sci* **29**, 1069-1078 (2020). https://doi.org:10.1002/pro.3791

53 Liebschner, D. *et al.* Macromolecular structure determination using X-rays, neutrons and electrons: recent developments in Phenix. *Acta Crystallogr D Struct Biol* **75**, 861-877 (2019). https://doi.org:10.1107/S2059798319011471

54 Afonine, P. V. *et al.* Real-space refinement in PHENIX for cryo-EM and crystallography. *Acta Crystallogr D Struct Biol* **74**, 531-544 (2018). https://doi.org:10.1107/S2059798318006551

55 Wang, R. Y. R. *et al.* Automated structure refinement of macromolecular assemblies from cryo-EM maps using Rosetta. *Elife* **5** (2016). https://doi.org:ARTN e17219 10.7554/eLife.17219

56 Moriarty, N. W., Grosse-Kunstleve, R. W. & Adams, P. D. electronic Ligand Builder and Optimization Workbench (eLBOW): a tool for ligand coordinate and restraint generation. *Acta Crystallogr D Biol Crystallogr* **65**, 1074-1080 (2009). https://doi.org:10.1107/S0907444909029436

57 Williams, C. J. *et al.* MolProbity: More and better reference data for improved all-atom structure validation. *Protein Sci* **27**, 293-315 (2018). https://doi.org:10.1002/pro.3330

58 Barad, B. A. *et al.* EMRinger: side chain-directed model and map validation for 3D cryo-electron microscopy. *Nat Methods* **12**, 943-946 (2015). https://doi.org:10.1038/nmeth.3541

59 Afonine, P. V. *et al.* New tools for the analysis and validation of cryo-EM maps and atomic models. *Acta Crystallogr D Struct Biol* **74**, 814-840 (2018). https://doi.org:10.1107/S2059798318009324

60 Rao, S., Klesse, G., Stansfeld, P. J., Tucker, S. J. & Sansom, M. S. P. A heuristic derived from analysis of the ion channel structural proteome permits the rapid identification of hydrophobic gates. *Proc Natl Acad Sci U S A* **116**, 13989-13995 (2019). https://doi.org:10.1073/pnas.1902702116

61 Klesse, G., Rao, S., Sansom, M. S. P. & Tucker, S. J. CHAP: A Versatile Tool for the Structural and Functional Annotation of Ion Channel Pores. *J Mol Biol* **431**, 3353-3365 (2019). https://doi.org:10.1016/j.jmb.2019.06.003

62 Schrödinger, L. The PyMOL Molecular Graphics System, Version 2.1 Schrödinger, LLC.

63 Pettersen, E. F. *et al.* UCSF Chimera--a visualization system for exploratory research and analysis. *J Comput Chem* **25**, 1605-1612 (2004). https://doi.org:10.1002/jcc.20084

64 Goddard, T. D. *et al.* UCSF ChimeraX: Meeting modern challenges in visualization and analysis. *Protein Sci* **27**, 14-25 (2018). https://doi.org:10.1002/pro.3235

611 65 Sievers, F. *et al.* Fast, scalable generation of high-quality protein multiple sequence
612 alignments using Clustal Omega. *Mol Syst Biol* **7**, 539 (2011).
613 https://doi.org:10.1038/msb.2011.75
614 66 Robert, X. & Gouet, P. Deciphering key features in protein structures with the new
615 ENDscript server. *Nucleic Acids Res* **42**, W320-324 (2014).
616 https://doi.org:10.1093/nar/gku316
617

Figures

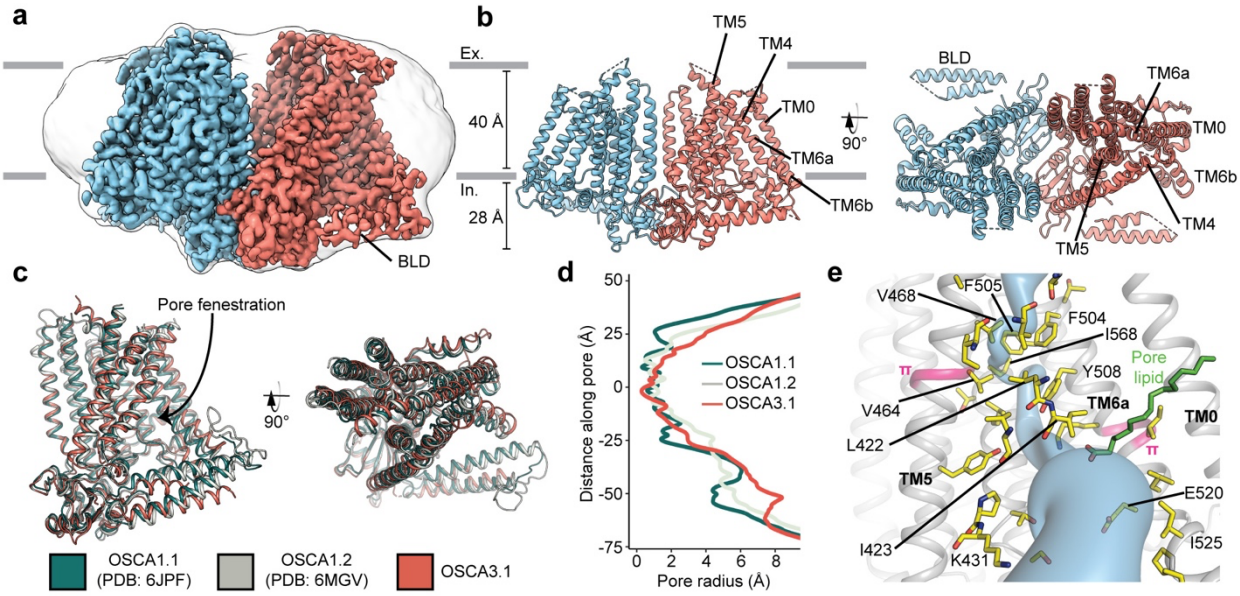

Figure 1: Cryo-EM structure and pore of OSCA3.1.
a, Cryo-EM map of OSCA3.1 dimer colored by subunit. Nanodisc density in grey corresponds to the unsharpened map (gaussian-filtered to 1.5 σ). **b,** Front (left) and top (right) view of atomic model. Ex.: Extracellular, In.: Intracellular. **c,** Superposition of OSCA1.1, OSCA1.2 (in nanodiscs) and OSCA3.1 protomers. **d,** Pore profile of OSCAs in **c**. **e,** View of the pore pathway (blue) of OSCA3.1. Pore facing residues colored in yellow, with selected residues labeled. π-helical turns in pink. Putative pore lipid in green. Backbone of TM3 and TM4 helices hidden for clarity.

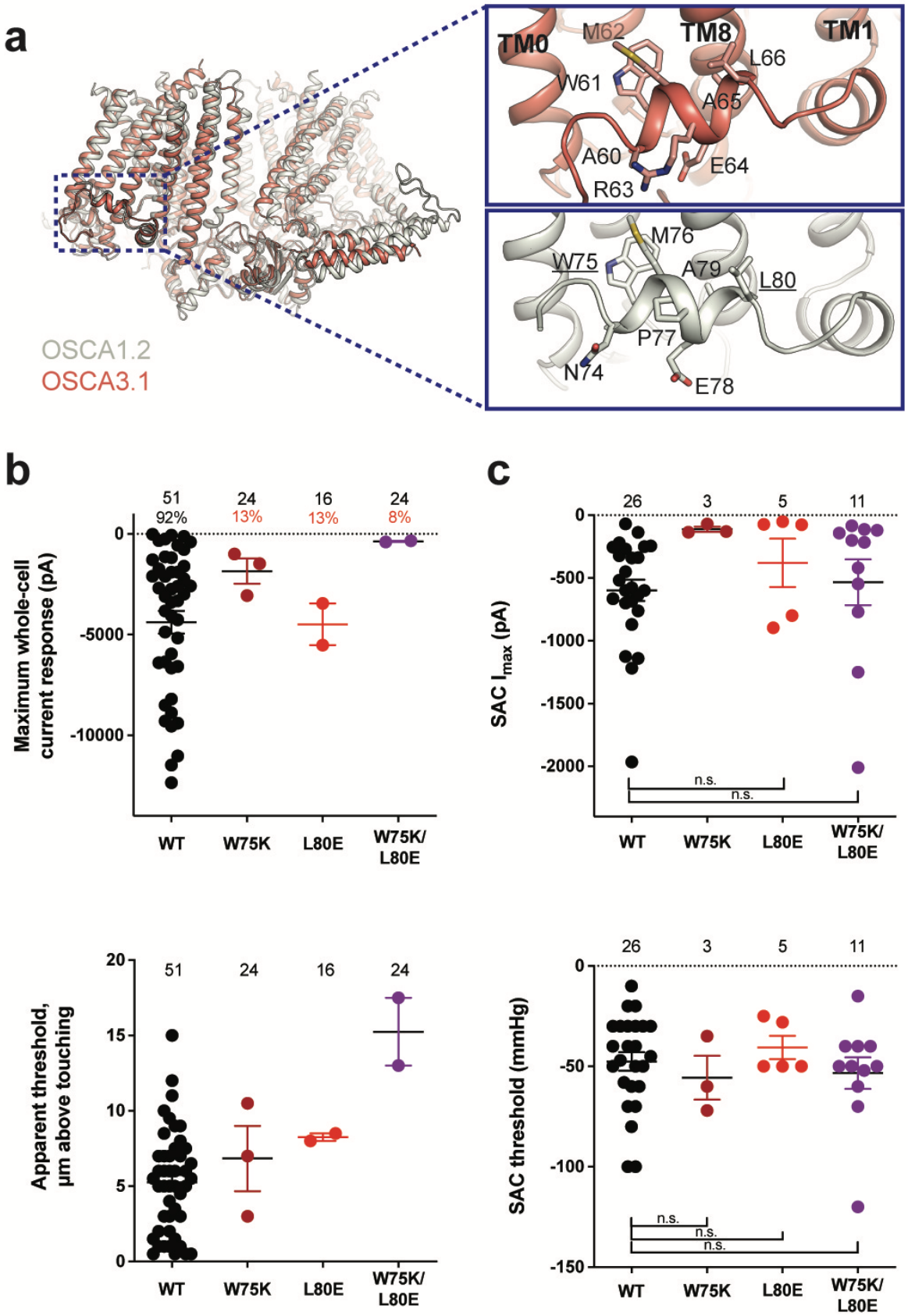
a
TM0
M62
TM8
TM1
L66
W61
A65
A60
E64
R63
M76
W75
A79
L80
P77
N74
E78
OSCA1.2
OSCA3.1
b
51
92%
24
13%
16
13%
24
8%
Maximum whole-cell current response (pA)
0
-5000
-10000
WT
W75K
L80E
W75K/ L80E
c
26
3
5
11
SAC I_{max} (pA)
0
-500
-1000
-1500
-2000
n.s.
n.s.
WT
W75K
L80E
W75K/ L80E
51
24
16
24
Apparent threshold, µm above touching
20
15
10
5
0
WT
W75K
L80E
W75K/ L80E
26
3
5
11
SAC threshold (mmHg)
0
-50
-100
-150
n.s.
n.s.
n.s.
WT
W75K
L80E
W75K/ L80E

Figure 2: Amphipathic helix mutants of OSCA1.2.
a, Superposition of OSCA1.2 (grey) and OSCA3.1 (red). Insets: close-up view of amphipathic helix. Residues substituted in OSCA1.2 for electrophysiology experiments are underlined. **b,** Few cells expressing mutations in the amphipathic helix respond to poking compared to WT controls. Top panel: Maximum poke-induced currents observed in whole-cell mode for cells exposed to displacements up to 8.9 ± 0.6 µm (N=51; mean ± S.E.M.), 12.8 ± 0.7 µm (N=24), 12.4 ± 0.7 µm (N=16), and 12.8 ± 0.5 µm (N=24) above touching for WT, OSCA1.2$_{W75K}$, OSCA1.2$_{L80E}$, and OSCA1.2$_{W75K/L80E}$, respectively. Bottom panel: the apparent threshold in µm above touching the cell for this cohort. **c,** SAC maximal current (I_{max}) (top) and mmHg threshold (bottom) from WT and OSCA1.2$_{W75K/L80E}$-expressing cells reveal no significant differences in the ability of negative pressure to activate channels in cell-attached patches (Student's *t*-test). Also shown are data from single mutants OSCA1.2$_{W75K}$ and OSCA1.2$_{L80E}$. Too few patches were obtained for OSCA1.2$_{W75K}$ to compare I_{max}. Electrode resistances for **c** were similar in all cases (WT: 2.3 ± 0.1 MΩ (N=26); W75K: 2.1 ± 0.4 MΩ (N=3), L80E: 2.2 ± 0.1 MΩ (N=5), W75K/L80E: 1.8 ± 0.1 MΩ (N=11)). For panels **b-c**: individual cells are represented as scatter points; mean and S.E.M. are displayed.

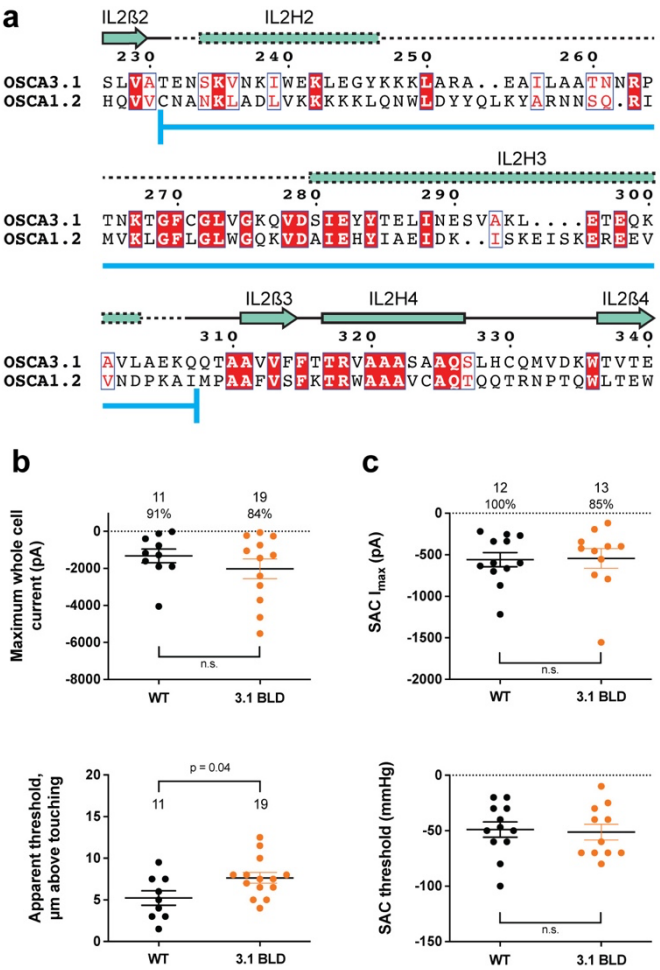

Figure 3: OSCA1.2$_{OSCA3.1\text{-}BLD}$ chimera.
a, Amino acid sequence alignment of the BLD region of OSCA1.2 and OSCA3.1. Full alignment in **Supplementary Fig. 3.** Blue line at bottom of sequences denotes the sequence swapped in OSCA1.2$_{OSCA3.1\text{-}BLD}$ chimera. **b,** Poke-induced responses are observed in HEK-P1KO cells expressing OSCA1.2$_{3.1\text{-}BLD}$. Top panel: Maximum poke-induced currents observed in whole-cell mode for cells exposed to displacements up to 9.8 ± 0.8 µm (N=11; mean ± S.E.M.) and 11.8 ± 0.6 µm (N=19) above touching for WT and OSCA1.2$_{3.1\text{-}BLD}$, respectively. The percentage of cells with responses are shown above. Bottom panel: the apparent threshold in µm above touching the cell for this cohort. **c,** SAC I_{max} (top) and mmHg threshold (bottom) from WT and OSCA1.2$_{3.1BLD}$-expressing cells reveal similar activity induced by negative pressure in cell-attached patches. Data shown were obtained from the same experiments. Electrode resistances for **c** were similar in all cases (WT: 2.4 ± 0.1 MΩ (N=12); OSCA1.2$_{OSCA3.1\text{-}BLD}$: 2.5 ± 0.1 MΩ (N=13)).

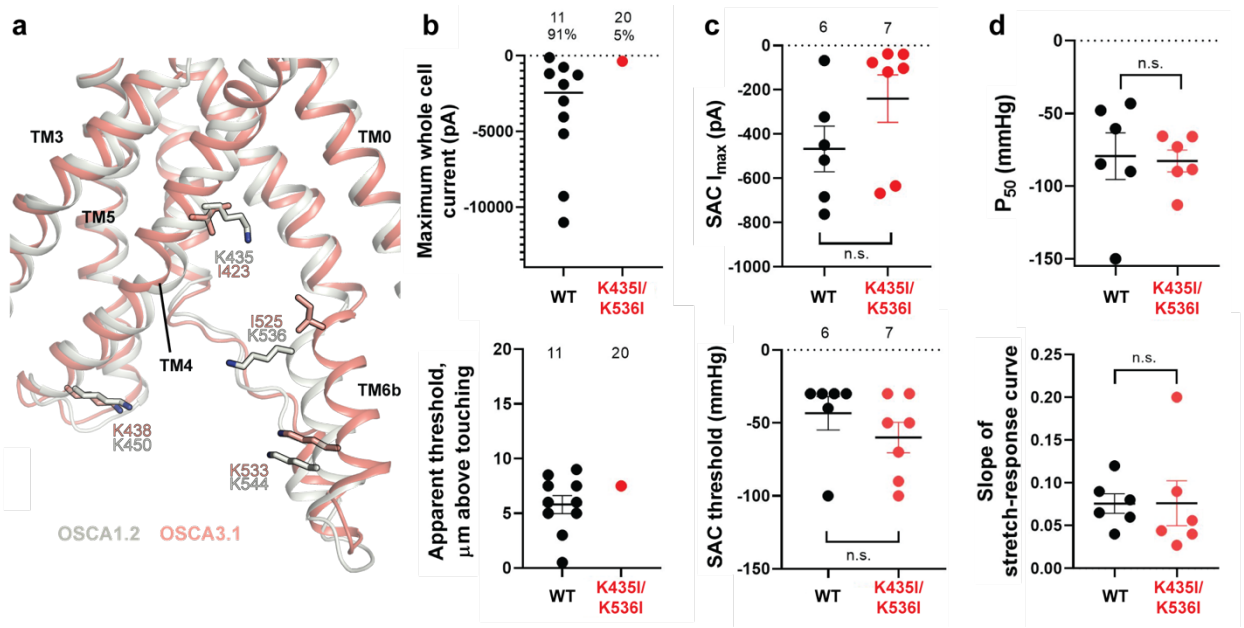

Figure 4: Probing the functional role of the potential lipid-interacting residues. **a,** Superposition of OSCA1.2 and OSCA3.1 around the pore fenestration. Residues of OSCA1.2 predicted to interact with lipids and corresponding residues in OSCA3.1 are shown. **b,** Few OSCA1.2$_{K435I/K536I}$ -expressing HEK-P1KO cells respond to the poke stimulus while nearly all cells expressing OSCA1.2 WT channels respond (percentages shown above under the N of cells tested). Top panel: Maximum poke-induced currents observed in whole-cell mode for cells exposed to displacements up to 9.7 ± 1 µm (N=11; mean ± S.E.M.) and 12.1 ± 0.6 µm (N=20) above touching for WT and OSCA1.2$_{K435I/K536I}$, respectively. Bottom panel: the apparent threshold in µm above touching the cell for this cohort. **c,** SAC Imax (top) and mmHg threshold (bottom) from WT and OSCA1.2$_{K435I/K536I}$-expressing cells reveal no significant differences in the ability of negative pressure to activate channels in cell-attached patches (Student's *t*-test). Electrode resistances were similar in all cases (WT: 2.1 ± 0.2 MΩ (N=10); K435I/K546I: 1.7 ± 0.3 MΩ (N=7)). Data were collected within 15 min of exposure of cells to high K+ used in this assay. **d,** Analysis of stimulus-response relationships reveal no significant differences (Student's *t*-test) in pressure to half-maximal activation (P_{50}; top) or the slope of the curve (bottom). Whole cell and SAC data were obtained from cells transfected at the same time.

Supplemental figures

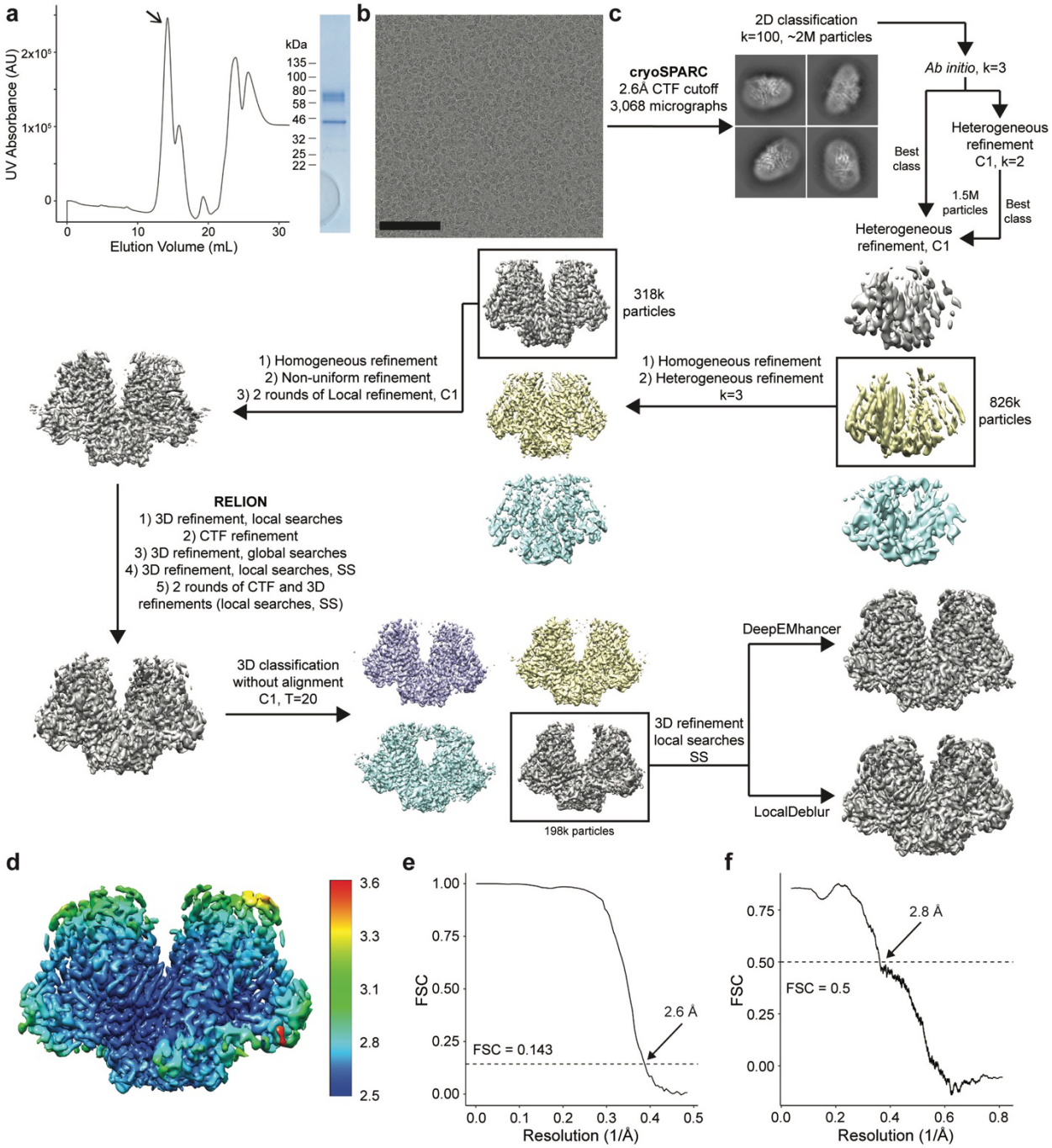

Supplementary Figure 1: Purification and cryo-EM data processing of OSCA3.1. **a,** SEC trace (left) from OSCA3.1 reconstitution in nanodiscs. Arrow points to peak corresponding to fractions pooled and ran on SDS-PAGE (right). Molecular weight of OSCA3.1 and MSP2N2 is approximately 82kDa and 43kDa, respectively. **b,** Representative cryo-EM micrograph. Black bar is 100nm. **c,** Cryo-EM processing workflow. C2 symmetry was imposed during refinements unless otherwise specified. 3D refinements in RELION were performed using the SIDESPLITTER algorithm where

indicated (SS). **d,** LocalDeblur map colored by local resolution calculated in RELION. **e,** FSC plot calculated in RELION. **f,** LocalDeblur map to model FSC plot.

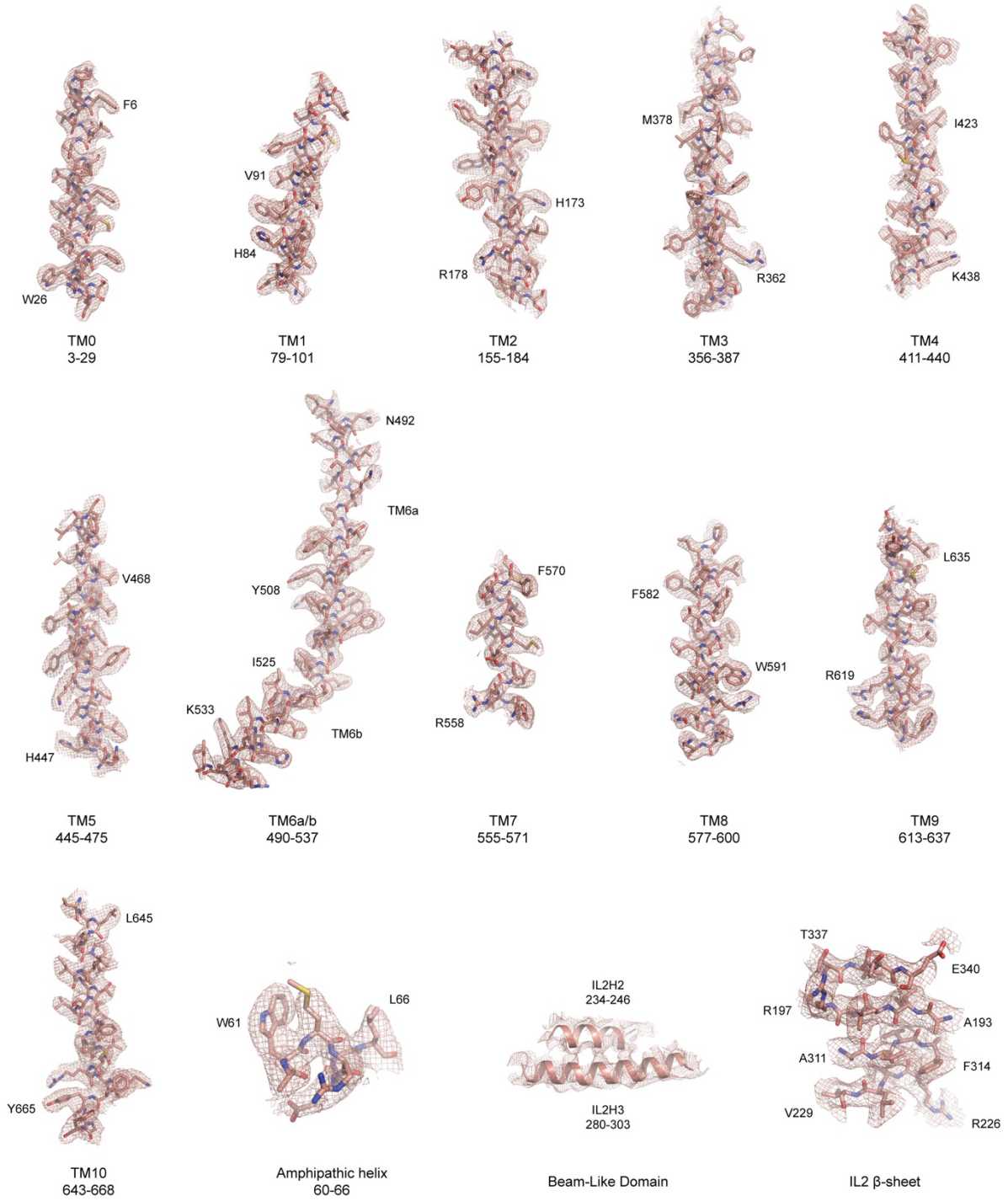

Supplementary Figure 2: Fit of OSCA3.1 model to LocalDeblur map.
Fit of OSCA3.1 model to selected regions of the LocalDeblur map. Map was contoured at a threshold of 2 (for the BLD) or 4 σ.

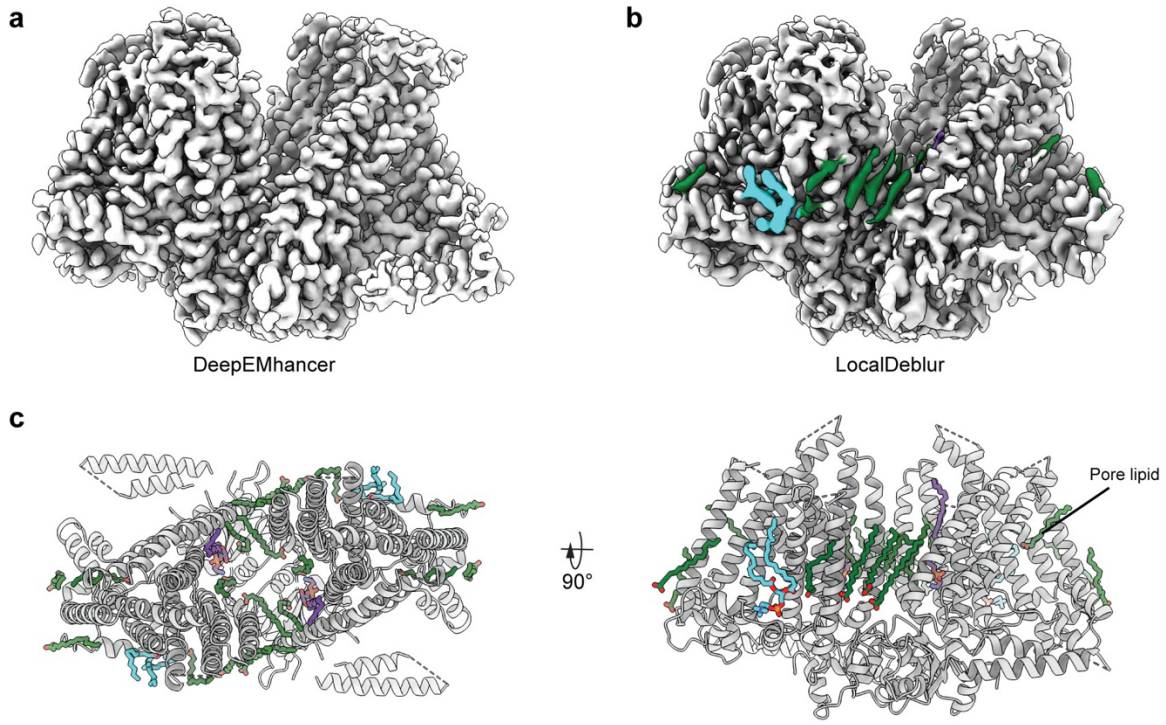

Supplementary Figure 3: Comparison of DeepEMhancer and LocalDeblur postprocessed maps.
a, DeepEMhancer map. **b,** LocalDeblur map with lipid-like densities colored. **c,** Top (left) and front (right) view of OSCA3.1 model with modelled lipids. Lipids were tentatively modelled as palmitic acid (green), phosphatidylcholine (cyan), and lyso-phosphatidylcholine (purple).

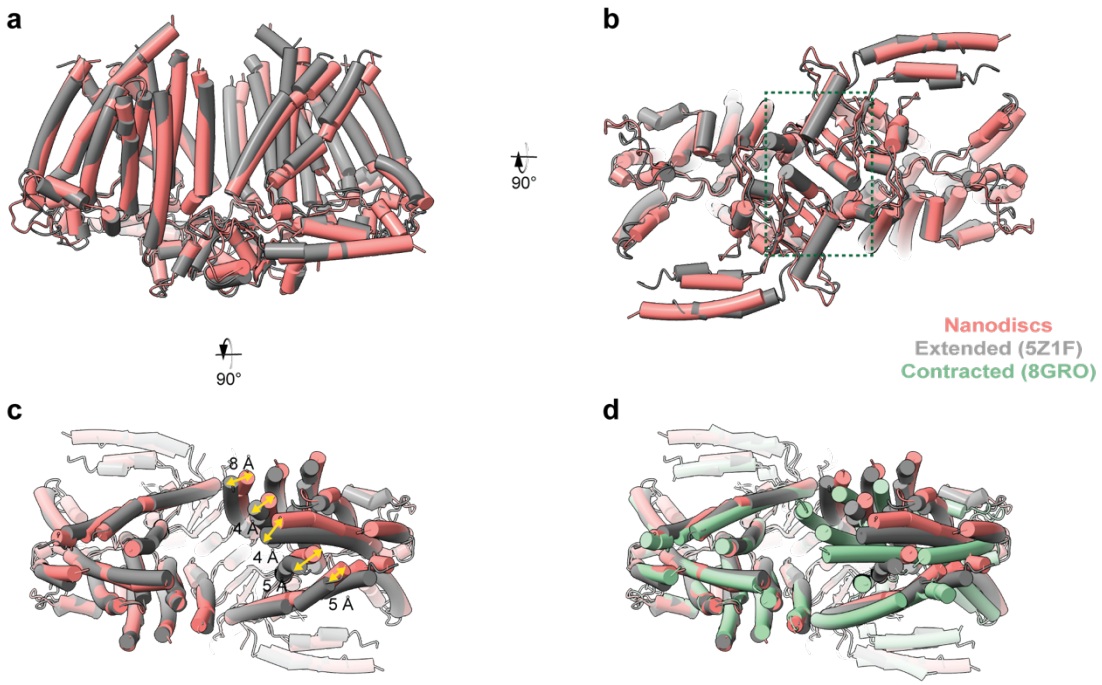

Supplementary Figure 4: Comparison of OSCA3.1 in nanodiscs and detergent states.
a, Front view of model superposition of OSCA3.1 in nanodiscs and extended state in digitonin (PDB: 5Z1F). Alignment done on left protomer. **b,** Intracellular view. Dimerization domain is enclosed in a green square. **c,** Extracellular view illustrating shifts of the nanodisc sample towards the outer edges, and increasing the distance between the two protomers in the inter-subunit cleft. **d,** Extracellular view of the OSCA3.1 in nanodiscs, extended state in digitonin, and contracted state in LMNG (PDB: 8GRO).

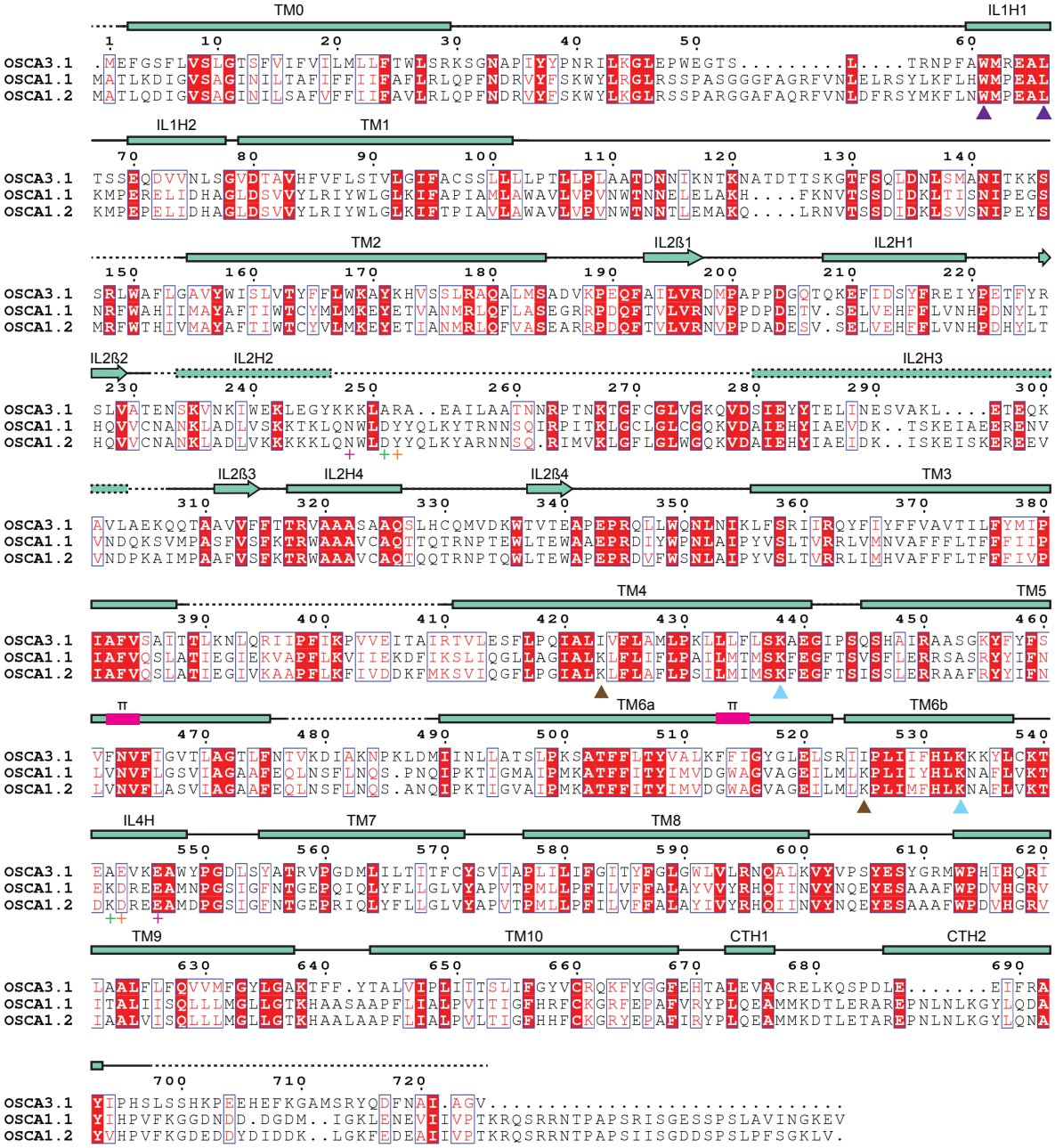

Supplementary Figure 5: Protein sequence alignment of OSCA3.1.
Amino acid sequence alignment of *Arabidopsis thaliana* OSCA3.1, OSCA1.1 and OSCA1.2. Secondary structure of OSCA3.1 represented on top, where rectangles represent α helices and arrows β strands. Dashed lines correspond to regions not modelled. π-helical turns labeled in magenta. IL2H2 and IL2H3 were modelled as poly-Ala and the registry was assigned tentatively. Purple arrowheads point to residues in the amphipathic helix that were mutated in OSCA1.2 for electrophysiology experiments. Predicted lipid-interacting residues denoted by light blue (conserved between OSCA1.2 and OSCA3.1) or brown (not conserved) arrowheads. Evolutionarily coupled residues

marked by plus sign (+), with each pair having the same color. TM: Transmembrane; IL: Intracellular Loop; CT: C-terminal; H: Helix; ß: ß-strand.

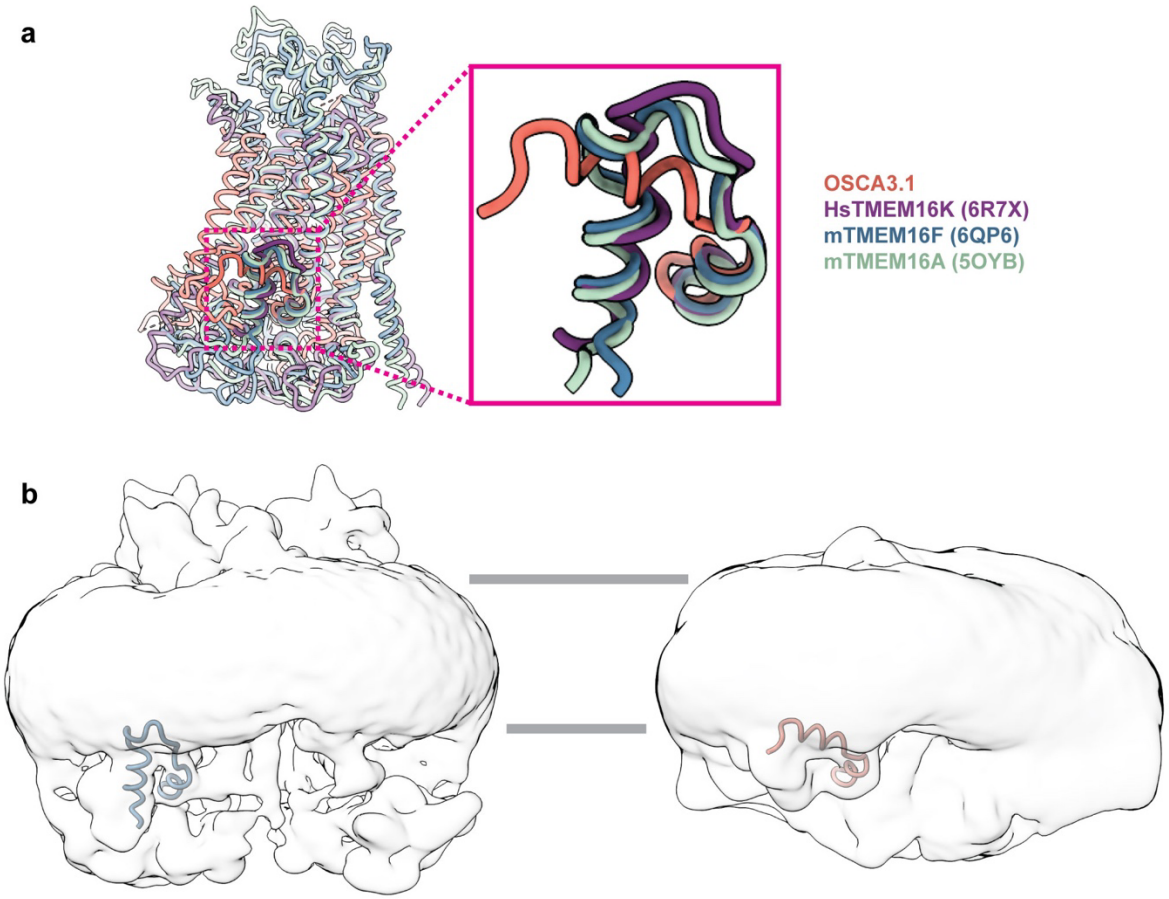

Supplementary Figure 6: Comparison of amphipathic helix of OSCA3.1 with corresponding helices in TMEM16 structures.
a, Superposition of one protomer of OSCA3.1 and selected members of the homologous TMEM16 family. Inset: zoom-in view of amphipathic helix of OSCA3.1 and homologous intracellular helix of TMEM16 homologs. Hs: *Homo sapiens*; m: mouse. **b,** EM density of mTMEM16F (left, EMDB: 4611) and unsharpened density of OSCA3.1 (right) showing position of respective helices shown in **a**. A gaussian-filter of 2 σ was applied to the densities. Horizontal gray lines denote the approximate position of the membrane bilayer.

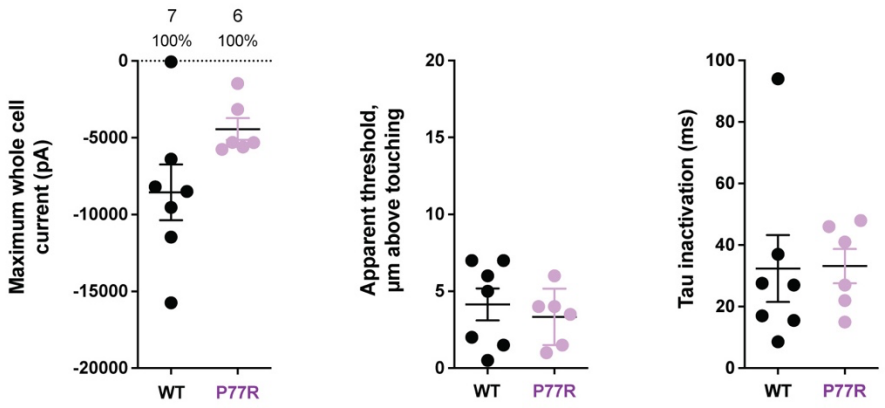

Supplementary Figure 7: Poke-induced response of OSCA1.2$_{P77R}$.
Introduction of arginine from OSCA3.1 into the OSCA1.2 background did not alter the poke-induced response. Left panel: Maximum poke-induced whole-cell currents observed for cells exposed to displacements up to 7.2 ± 1.4 µm (N=7; mean ± S.E.M.) and 6.5 ± 0.6 µm (N=6) above touching for WT and OSCA1.2$_{P77R}$, respectively. Center panel: the apparent threshold in µm above touching for the cells in this cohort. Right panel: Time constant of inactivation of currents elicited in the cells in this cohort.

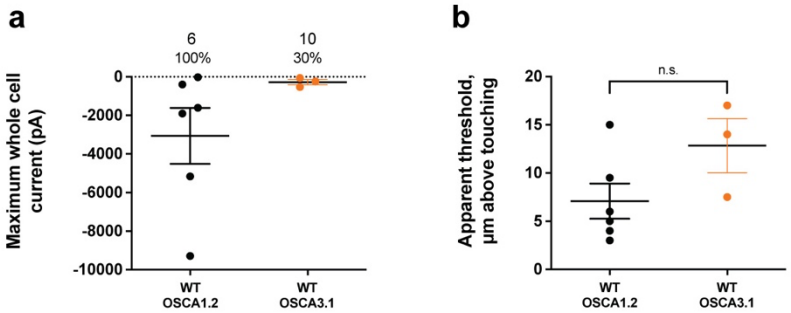

Supplementary Figure 8: OSCA3.1 may be poke-sensitive at high thresholds. Poke-induced whole-cell current responses are observed in HEK-P1KO cells expressing OSCA3.1. **a,** Maximum poke-induced currents observed in whole-cell mode for cells exposed to displacements up to 10.4 ± 1.2 µm (N=6; mean ± S.E.M.) and 13.8 ± 0.9 µm (N=3) above touching for $OSCA1.2_{WT}$ and $OSCA3.1_{WT}$, respectively. Although 6 of 6 OSCA1.2 expressing cells responded to poking, only 3 of 10 showed a response before the disruption of the recording. **b,** The apparent threshold in µm above touching the cell for this cohort.

148 **Supplementary Table 1. Data collection, processing, model refinement and**
149 **validation.**

	OSCA3.1
Data collection and processing	
Magnification	29000
Voltage (kV)	300
Electron exposure (e–/Å^2)	50
Defocus range (μm)	-0.4 to -1.5
Pixel size (Å)	1.03
Initial particle images (no.)	1,913,316
Symmetry imposed	C2
Final particle images (no.)	197,944
Map resolution (Å)	2.6
FSC threshold	0.143
Map sharpening *B* factor (Å^2)	-64
Model	
Composition	
Peptide chains	2
Protein residues	1148
Ligands	24
R.m.s. deviations	
Bond lengths (Å)	0.023
Bond angles (°)	1.677
Validation	
MolProbity score	0.74
Clashscore	0.74
EMRinger score	4.12
Poor rotamers (%)	0.00
Ramachandran plot	
Favored (%)	98.93
Allowed (%)	1.07
Disallowed (%)	0.00
Deposition ID	
EMDB	41911
PDB	8U53

150